

Cite this: *Phys. Chem. Chem. Phys.*, 2012, **14**, 13350–13364

[www.rsc.org/pccp](http://www.rsc.org/pccp)

PAPER

## Barrierless photoisomerisation of the “simplest cyanine”: Joining computational and femtosecond optical spectroscopies to trace the full reaction path<sup>†</sup>

Alexander Weigel,<sup>a</sup> Matthias Pfaffe,<sup>a</sup> Mohsen Sajadi,<sup>a</sup> Rainer Mahrwald,<sup>a</sup> Roberto Improta,<sup>b</sup> Vincenzo Barone,<sup>c</sup> Dario Polli,<sup>d</sup> Giulio Cerullo,<sup>d</sup> Nikolaus P. Ernstd<sup>\*a</sup> and Fabrizio Santoro<sup>\*e</sup>

Received 11th May 2012, Accepted 16th July 2012

DOI: 10.1039/c2cp41522d

The photoisomerisation of 1,1'-diethyl-2,2'-pyridocyanine, regarded by Brooker as the simplest cyanine, is examined in methanol by time-resolved experiments and PCM/TD-CAM-B3LYP calculations. Femtosecond transient absorption, fluorescence upconversion, and stimulated Raman scattering, all with broadband coverage, provide a panoramic view of the photoreaction. On the computational side, evolving distributions on an  $S_1$  minimum-energy path are obtained by solving the Smoluchowski equation for drift and diffusion of torsional motion. Absorption and fluorescence bandshapes are calculated and compared to the observations; near-quantitative agreement implies that the entire  $S_1$  path has been observed. Most importantly the global  $S_1$  minimum, *i.e.* the perpendicular “phantom state”  $P^*$ , can be identified and characterized in this way. Internal conversion of  $P^*$  (3.7 ps), assisted by solvent equilibration, leads to the hot ground state. Within 5 ps, vibrational bands of *cis* and *trans* isomers are recognized with the help of calculated Raman spectra. The differences between observed and simulated spectra are discussed.

### 1. Introduction

Cyanines represent a large and diverse family of dyes which was discovered more than 150 years ago, when cornflower-blue 1,1'-diethyl-2,2'-cyanine (1122-C, pseudoisocyanine PIC) was first synthesized.<sup>1</sup> Their dominant use as photosensitizers is related to aggregation;<sup>2</sup> more recently the nonlinear optical properties became important.<sup>3</sup> Structural transformations of

proteins and nucleic acids can be monitored by cyanine fluorescence.<sup>4,5</sup> An exhaustive list of cyanine studies would appear daunting, and this is why only the most recent reviews and references are given here.

The electronic chromophore of cyanines consists essentially of two nitrogen centers ( $R_2N^+=$ ) and ( $-NR_2$ ) which are linked by an odd number of methine groups ( $=CH-$ ). The nitrogen centers are part of carbocyclic or heterocyclic systems, as shown by representative structures in Scheme 1. Intense color in a narrow spectral range can be tuned by varying the chain length. Other features of the structure (symmetric or asymmetric, open-chain or partly closed, different atomic centers) allow wide changes in the electronic properties, such as dipole moments, band widths, and fluorescence yields.<sup>6</sup>

Notwithstanding the large variety of cyanines, the pathway from the bright emissive Franck–Condon (FC) region of excited state  $S_1$  back to the electronic ground state  $S_0$  has common features.<sup>7–12</sup> On the  $S_1$  potential energy surface (PES), *trans*–*cis* isomerisation around C–C bonds in the polymethine chain leads to a perpendicular structure  $P^*$ . There a conical intersection (CI) seam with  $S_0$  opens an extremely efficient channel for internal conversion. Afterwards the system continues its evolution in  $S_0$  to form the isomer. The barrierless path depends sensitively on the active volume and solvent viscosity, and therefore the deactivation efficiency or

<sup>a</sup> Department of Chemistry, Humboldt-Universität zu Berlin, Brook-Taylor-Strasse 2, 12489 Berlin, Germany.

E-mail: nernst@chemie.hu-berlin.de

<sup>b</sup> CNR–Consiglio Nazionale delle Ricerche, Istituto di Biostrutture e Bioimmagini (IBB-CNR), Via Mezzocannone 16, 80134 Napoli, Italy

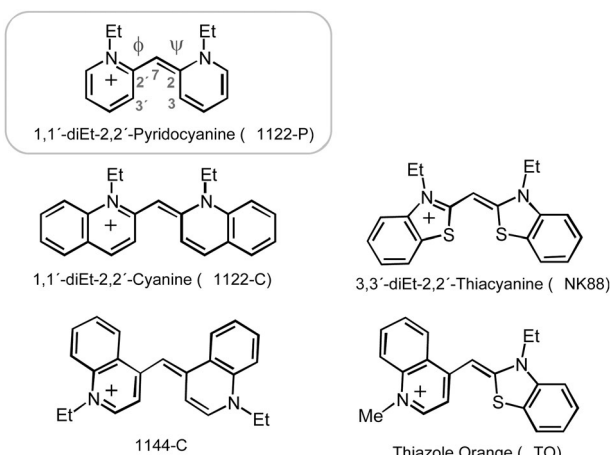
<sup>c</sup> Scuola Normale Superiore, piazza dei Cavalieri 7, 56126 Pisa, Italy

<sup>d</sup> IFN-CNR, Dipartimento di Fisica, Politecnico di Milano, p.zza Leonardo da Vinci 32, 20133 Milano, Italy

<sup>e</sup> CNR–Consiglio Nazionale delle Ricerche, Istituto di Chimica dei Composti OrganoMetallici (ICCOM-CNR), UOS di Pisa, Area della Ricerca, Via G. Moruzzi 1, I-56124 Pisa, Italy.

E-mail: fabrizio.santoro@iccom.cnr.it

† Electronic supplementary information (ESI) available: Experiments: details on the synthesis of 1122-P; “species” associated spectra of SE; comparison of SE and TA signals. Computations: additional computational details; Tables S1 and S2 reporting B3LYP results; stationary structures of 1122-P; MEP of Me-1122-P in gas phase; FC|VG absorption spectra and detailed analysis of vRR spectra together with sketches of the most important vibrations for *trans*, *cis* and *dcis* isomers. Details on the solution of the Smoluchowski equation. See DOI: 10.1039/c2cp41522d



**Scheme 1** The pyridocyanine (box) studied here. Dihedral angles  $\phi = 2-7-2'-3'$  and  $\psi = 2'-7-2-3$  describe the deviation from the *all-trans* conformation. Other cyanines which have been investigated with femtosecond spectroscopy are also shown.

conversely, the fluorescence yield, may be used to probe the state of the environment in biolabeling applications.

Quantum-chemical calculations provided further details on the excited-state reaction.<sup>10–12</sup> CASSCF calculations for open-chained  $\text{H}_2\text{N}^+ = \text{CH}-\text{CH}=\text{CH}-\text{NH}_2$  gave the following picture:<sup>10</sup> Optical absorption  $\text{S}_1 \leftarrow \text{S}_0$  initially causes symmetric expansion and conrotatory twisting ( $\phi = \psi$ , see Scheme 1) until  $\phi \approx 80^\circ$ . Then asymmetric stretching of the bonds sets in, strongly increasing with further conrotation, and the positive charge becomes localized on one of the two moieties. After the perpendicular conformation is reached, the bridge plane turns coplanar with the charged moiety (described by disrotatory motion) to reach the global excited state minimum  $\text{P}^*$ . For the fused-ring NK88 cyanine in solution, time-dependent DFT (TD-DFT) calculations showed that the change from conrotary to disrotatory motion takes place much earlier (closer to planarity,  $\phi \approx 20^\circ$ ).<sup>11</sup> Internal conversion is an activated process in both cases, involving asymmetric stretching from the global minimum to a CI.<sup>10,11</sup>

Femtosecond optical spectroscopy has been performed for the short-chain cyanines<sup>13–26</sup> which are shown below the box in Scheme 1. Following ultrafast  $\text{S}_1 \leftarrow \text{S}_0$  excitation in solution, the decay of excited-state absorption  $\text{S}_n \leftarrow \text{S}_1$  and stimulated emission  $\text{S}_1 \rightarrow \text{S}_0$  was compared to the recovery of ground-state absorption. A recent study of 1144-C<sup>22</sup> suggests fast migration as well as broadening of the wavepacket on the  $\text{S}_1$  surface on the sub-ps time scale, followed by slower population decay to the  $\text{S}_0$  state (7 ps). On balance, experiments on cyanine thus show that two mechanisms of  $\text{S}_0$  recovery should be distinguished: a fast ( $\sim 1$  ps) direct contribution after passage through the CI, and a slow ( $\sim 10$  ps) indirect contribution from the ground-state isomer, by thermal back-reaction over a barrier.

As a matter of fact, a full picture of the barrierless photoisomerisation cannot be found by observations alone, and quantum-chemical calculations of the participating PES are necessary to understand the observations. Usually the comparison of observed and computed data is performed qualitatively – in this way the remarkable progress in our knowledge of the underlying mechanisms was made, as sketched above.

On the other hand the full potential of the experimental and computational data combined, to unveil the fine details of the investigated process, is clearly not exhausted by such a qualitative approach. A degree of uncertainty in the interpretation of the observations is left since, without explicit simulations of the spectroscopic signals, it can be “reasonably guessed” but not “proved” that they are explained by the computational data.

A quantitative link between observation and computational modeling of ultrafast photoinduced processes requires, in principle, fully quantum-dynamical simulations. Unfortunately that approach still represents a huge challenge for the real molecular systems which are measured in practice. It is therefore desirable to use an alternative approach, and this prompted our study. Specifically, we investigate here whether an integrated computational model made up by the characterisation of minimum-energy paths (MEP), classical evolution of the photoexcited distribution along the MEP, and quantum simulation of vibronic spectra at relevant points of the MEP, allows a quantitative description of the spectroscopic signals and their time evolution.

To this aim we selected 1,1'-diethyl-2,2'-pyridocyanine (1122-P in Scheme 1)<sup>27–38</sup> which Brooker regarded as “the simplest cyanine”.<sup>28</sup> Quantum-chemical calculations are greatly facilitated for this dye molecule, compared to the others in Scheme 1. Computed and observed spectra should therefore correspond most closely, a pre-requisite for our purpose. The idea is to observe and define transient states by different optical spectroscopies to highest accuracy, and then to look for computed counterparts. The photoisomerization in methanol is observed by three kinds of femtosecond experiments: transient absorption,<sup>39</sup> broadband fluorescence upconversion,<sup>40</sup> and stimulated Raman scattering.<sup>41</sup> All have broad spectral coverage with high temporal (30–130 fs) and spectral resolution. Characteristic transient states are defined by associated spectra that result from a joint analysis of the three measured evolutions. The PESs of the relevant electronic states and optical spectra are computed by cost-effective time-dependent DFT calculations (CAM-B3LYP functional<sup>42,43</sup>), accounting for solvent effects with the polarizable continuum model (PCM).<sup>44</sup>

In order to link the different optical observations to the calculated PESs in a semi-quantitative manner, (i) harmonic representations are used at critical points along the MEP to compute vibronic spectra, and (ii) the evolution of the photo-excited distribution along that path is treated as drift and diffusion, by solving the Smoluchowski equation for torsional motion. Two steps in the evolution of  $\text{S}_1$  are distinguished experimentally: decay and red-shift of emission with 0.13 ps time constant, and decay of weak emission with 0.88 ps time constant, corresponding to the creation of a faint broad absorption which peaks at 1.8 ps. The stationary absorption and transient fluorescence bandshapes agree near-quantitatively with experiments after adjusting the friction constant and correcting the transition energy once (*i.e.* the energy along the whole MEP has been shifted by the same value), because of inaccuracies of the TD-DFT/CAM-B3LYP calculations. In this way the entire calculated  $\text{S}_1$  path can be mapped to the experimental transient spectral features mentioned above. Most importantly, our procedure allows us to extract the transient absorption spectrum due to population at the

“perpendicular” global minimum P\*. Internal conversion from there generates hot S<sub>0</sub> absorption, providing resonance for fs Raman scattering. With the help of calculated Raman spectra, vibrational bands of *cis* and *trans* isomers are recognized at 5 ps. Thus, our combined approach leads to a detailed understanding of this cyanine dye. More generally it establishes a viable computational model for photochemical events characterized by a separation of dynamical regimes between classical (slow) and quantum (fast) structural motions. These are reflected in the time evolution of the electronic band positions and of their vibronic features, respectively.

The paper is organized as follows. Following a brief Section 2 on materials and methods, we report in Section 3 the spectroscopic results and quantum-chemical calculations separately. Their connection is established in Section 4 and open points are discussed in Section 5. We conclude in Section 6 with a summary and a caveat.

## 2. Materials and methods

### 2.1 Experiments

**Synthesis.** 1,1'-Diethyl-2,2'-pyrido cyanine iodide (CAS 16521-08-7 and 23664-32-6) was synthesized following ref. 28 [see ESI†]. The solvent for all measurements was spectrograde methanol. The stationary absorption<sup>30,34,35</sup> spectrum is shown in Fig. 1 for the conditions of our transient experiments. At maximum optical density OD ≈ 0.8 over 350 μm, association leads to 4% deviation from the Lambert–Beer law at the absorption peak and less to the blue.

*Transient absorption (TA) spectra* were recorded with optical pumping at 442 nm, on the high-energy side of the S<sub>1</sub> ← S<sub>0</sub> absorption band. A broad spectral range was probed by a time-delayed supercontinuum;<sup>39</sup> the maximal bleach signal was ΔOD<sub>max</sub> = −0.160. The probe chirp was measured with the pure solvent and corrected for all following presentations. High-time-resolution spectra were induced with sub-10-fs pump

pulses at 495 nm, and broadband probe pulses were centered at 570 nm.<sup>45,46</sup> In this case the sample cell had 200 μm internal path length to minimize the effects of group velocity mismatch.

*Time-dependent fluorescence up conversion spectra (FLUPS)* were measured by broadband upconversion.<sup>40</sup> The sample solution, of 0.6 peak absorbance across 0.4 mm path length, was excited with 450 nm pulses (40 fs, 0.6 μJ, 500 Hz). Fluorescence was imaged to a spot of 0.6 mm diameter on a KDP crystal (0.3 mm thick). Type II sum-frequency generation was achieved with delayed 1320 nm pulses (40 fs, 60 μJ) having a tilted pulse front. Upconverted light was imaged into a fiber bundle, dispersed in a grating spectrograph, and registered with a CCD camera. Photometric calibration and time correction were performed with several dyes and mixtures.<sup>40</sup> As a result, transient fluorescence photon distributions over visible wavelengths were obtained with 132 fs time resolution and 4.7 nm spectral resolution (fwhm of Gaussian apparatus functions). They were transformed into the corresponding spectra for stimulated emission, for comparison.

*Femtosecond stimulated Raman spectra (FSRS)* were obtained as reported in ref. 41 and 47. Transient measurements were carried out by exciting at 480 nm with 600 nJ (“actinic pump”). For the stimulating probe, broadband pulses from a NOPA with 60 nJ energy were used. Narrow-band Raman pump pulses (500 nJ, 520 nm – vertical red line in Fig. 1) were applied coincident with the probe pulses. The frequency scale was calibrated with a shift standard. The spectral resolution is 12 cm<sup>−1</sup> (fwhm), and the absolute position of Raman peak maxima is accurate to 1–2 cm<sup>−1</sup>; relative frequency changes within a measurement can be followed with higher precision. Positive ordinate values in the figures correspond to Raman emission.

A broad background due to TA in FSRS must be distinguished from sharp Raman features, absorptive as well as emissive; both are caused by the Raman pump. The background does not stay constant when the Raman pump is applied because electronic resonance (which one seeks to enhance the signal) also leads to population transfer; therefore the background must be identified with the Raman pulses switched on. We use alternating Raman frequencies and digital lock-in techniques, in a self-consistent procedure which was described in the ESI of ref. 41 and 47. Spectral integration of the background gives a χ<sup>(5)</sup> intensity correlation function from which a time resolution of 70 fs (fwhm) is inferred.

The solvent (methanol) FSRS spectrum is measured separately. Then, with a solution of the dye, a ground state FSRS spectrum is obtained with Raman pump and probe pulses alone. It contains the solvent spectrum which is scaled and subtracted. The correction is carried out by minimizing the strong methanol bands at 1034, 1109, and 1454 cm<sup>−1</sup>. The extent of residuals is controlled by comparing measurements in different solvents. Transient FSRS spectra represent the difference which the actinic pulse induces, hence the aforementioned solvent spectrum vanishes in this case.

### 2.2 Quantum-chemical computations

As a model for 1122-P one may study the homologous 1,1'-dimethyl-2,2'-pyridocyanine (Me-1122-P), as proven in

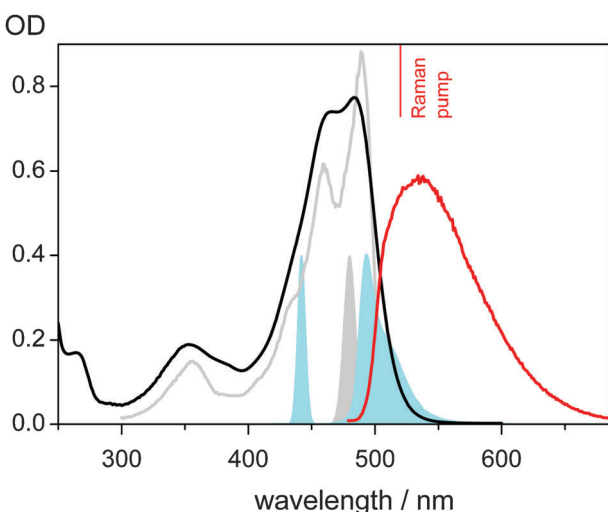


**Fig. 1** Stationary absorption spectrum of 1122-P in methanol (black), and the power spectra of pump pulses (from left: for transient absorption survey, actinic pump in FSRS, for 10 fs transient absorption). Red: fluorescence quantum distribution in ethanol at 90 K; gray: its excitation spectrum.

the ESI.<sup>†</sup> All quantum chemical calculations in this paper refer to the dimethyl compound unless mentioned otherwise, and have been performed by Gaussian 09.<sup>48</sup>

DFT and TD-DFT (for excited electronic states) levels of theory were used. For surveys of the PES we used the computationally convenient 6-31G(d) basis, while at relevant nuclear structures, energies were refined with the larger 6-311+G(2d,2p) set. The computational analysis is based mainly on the long-range corrected CAM-B3LYP functional, since it provides a reliable description of charge transfer (CT) transitions.<sup>42,43</sup> These are known to play a role in photoexcited cyanines, and the chosen functional should be adequate to treat a short-bridge cyanine like 1122-P (TD-DFT does not treat long-chain cyanines correctly,<sup>49,50</sup> though very encouraging results have been obtained by using some last generation functionals<sup>51</sup>). CAM-B3LYP results were checked with the widely-used B3LYP functional, which provides a qualitatively similar description of the PES (see ESI<sup>†</sup> for results) but for the aforementioned inaccuracy in regard to CT states.

Bulk solvent effects are included by PCM. For excited-state geometry optimizations we use the standard Linear Response implementation (LR-PCM) for which analytical energy gradients are available. At single points we also employed the recent State Specific (SS) PCM/TD-DFT implementation.<sup>52,53</sup> In this case the solvent polarization is equilibrated with the true charge density of the excited state, delivering more reliable results for CT states than LR-PCM/TD-DFT. For LR and SS single-point calculations we considered both equilibrium (*eq*) and nonequilibrium (*neq*) solvation regimes (see ESI<sup>†</sup> for further details). Excited-state optimizations were performed at the *eq* level.

Vibrationally resolved absorption and emission and vibrational resonance Raman (vRR) spectra of the *trans* isomer were computed including FC and Herzberg–Teller (HT) effects. In the initial and final electronic states the Hessian matrix was calculated at the respective equilibrium geometry (“adiabatic Hessian”, AH). To treat the Duschinsky effect we adopted the method FCclasses recently developed in our labs,<sup>54–57</sup> and its extension to deal with vRR spectra.<sup>58</sup> This method is implemented in open source codes<sup>59</sup> and available for absorption and emission in Gaussian09.<sup>60,61</sup>

For optical absorption and resonance Raman calculations of all isomers a simpler description of the excited-state PES was used. In this approach (i) HT effects are neglected, (ii) the normal modes and frequencies of  $S_1$  are taken to be equal to those of  $S_0$ , (iii) geometry displacements are derived from the  $S_1$  PES gradient at the equilibrium geometry of  $S_0$  (“vertical gradient”, VG) or obtained from  $S_1$  optimisation (“adiabatic shift”, AS).<sup>61</sup> As far as vRR spectra are concerned, they are then computed with Heller’s time-dependent theory in the short-time-dynamics (STD) limit.<sup>62</sup>

### 3. Results

#### 3.1 Experimental results

*Transient absorption spectra* are surveyed in Fig. 2. Within the first 320 fs after 442 nm excitation (time window a) one observes stimulated emission (SE,  $\Delta OD < 0$ ) in the fluorescence

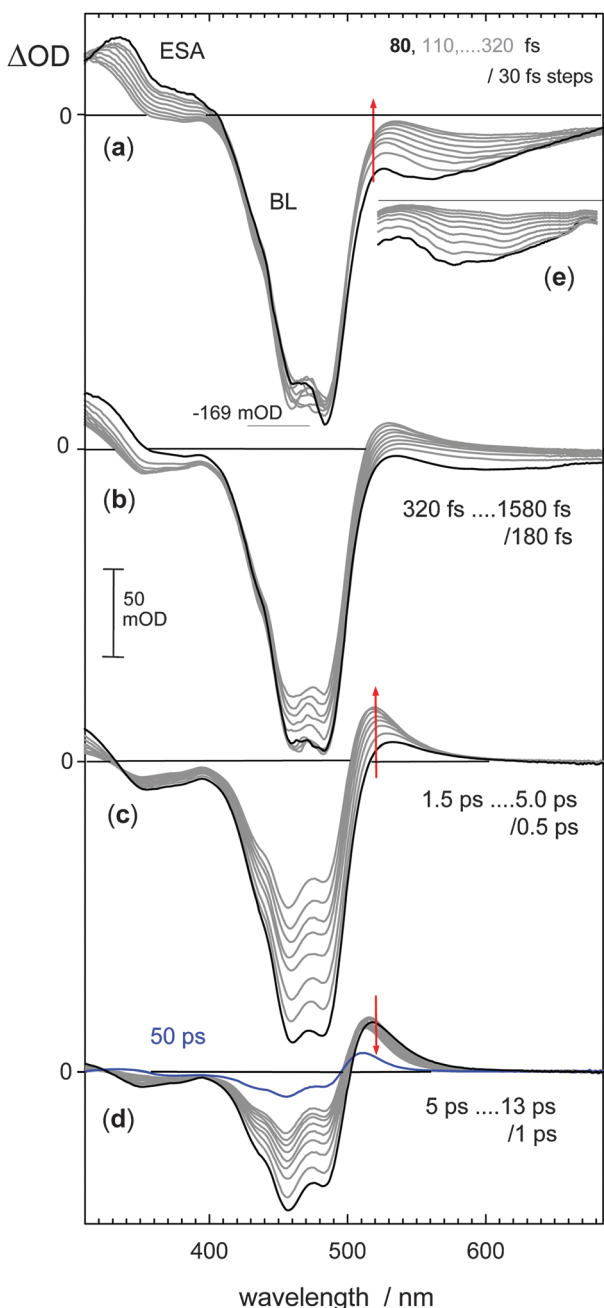


**Fig. 2** Transient absorption spectra of 1122-P in methanol after excitation at 442 nm (a–d; 86 fs fwhm of apparatus function). BL – bleached absorption  $S_1 \leftarrow S_0$ , SE – stimulated emission  $S_1 \rightarrow S_0$ , ESA – excited-state absorption  $S_n \leftarrow S_1$ , GSA – hot ground-state absorption. (e) Evolution upon 10 fs excitation at 495 nm (36 fs). Only the diffusive part (*i.e.* the result of a multiexponential global fit) is shown, at times as in (a). Arrows indicate the evolution, at the wavelength of the Raman pump in the FSRS experiments.

region (probe wavelengths longer than 520 nm). During this time the SE band decays while it shifts to the red and broadens; at the same time the excited-state absorption (ESA) around 350 nm decreases, whereas the ground-state bleach (BL) stays constant. Then within 1.5 ps (b) the SE band disappears, *i.e.* the induced optical density turns positive in the fluorescence region; at the same time the BL begins to decay.

These observations are consistent with internal conversion to a hot electronic ground state, which is characterized by a photoinduced ground state absorption (GSA) band around 525 nm. The latter grows to a maximum within 5 ps (c). Thereafter, slow decay (d) of both GSA and BL indicates ground-state vibrational cooling (see below).

The dynamics of the evolution was estimated by a multi-exponential global fit. Signal around time zero contains the so-called “coherent artifact” from Raman-type optical processes (this kind of information is exploited separately with the FSRS experiment). For the present analysis the coherence is described by a Gaussian time function  $G(t)$  together with its temporal derivatives  $G'(t)$  and  $G''(t)$ .<sup>39</sup> The sequential evolution is modeled by exponentials and a Heaviside function which have been convoluted with  $G(t)$ . Time constants obtained from the fit are 0.21, 3.7, 4.2, and 15.7 ps. The second and third time constants are both needed; they describe subtle spectral changes due to a ground-state intermediate as will be discussed.

High time resolution spectra were collected with red-edge excitation at 495 nm, which should result in lower vibrational temperature in  $S_1$ ; impulsive sub-10-fs excitation creates, in addition to excited state population, vibrational coherence. The SE spectrum now has weak vibronic structure which at 80 fs shows broad peaks at 581 and 603 nm, spaced apart by  $630\text{ cm}^{-1}$ , but this structure is close to the noise level and will therefore not be analysed later. A global multiexponential fit to the measured  $\Delta\text{OD}(\lambda,t)$  was performed at 500–680 nm, 0.05–1.5 ps, and this is shown as inset (e). Thus the diffusive (*i.e.* non-oscillatory) spectral evolution was obtained which is shown there. After subtraction of the fit from the measured data, temporal oscillations remain which depend on observation wavelength, indicating wavepackets in the excited and ground electronic states (see below).

*Time-resolved fluorescence spectra* are shown in Fig. 3a for delay times from 80 to 640 fs. For comparison with TA results, the measured distributions  $\partial\Phi/\partial\lambda$  (of  $\Phi$  photons over wavelength  $\lambda \propto \tilde{\nu}^{-1}$ ) were converted into  $(\partial\Phi/\partial\tilde{\nu})/\tilde{\nu}^2$  which is proportional to the cross section for SE. A global fit requires two exponential decay functions convoluted with the apparatus function; its quality can be appreciated from the fluorescence trace at 591 nm (panel Fig. 3b). The global fit may be interpreted using the following kinetic scheme: an initial fluorescent state relaxes ( $\tau_1 = 130$  fs) to a weakly emitting intermediate, from where the fluorescence disappears ( $\tau_2 = 880$  fs). The spectra associated with the initial and intermediate states are shown in Fig. S1 in ESI†; the peak position is seen to red shift by  $1340\text{ cm}^{-1}$  (red line). Combining these spectra with the relative populations (calculated from the kinetic scheme), a model for the SE spectrum is thus available for all wavelengths and times.

A femtosecond stimulated Raman scattering spectrum 5 ps after the actinic pump is shown in Fig. 4a (black line). The actinic  $S_1 \leftarrow S_0$  excitation has removed initial population for the stimulated Raman process, and therefore the FSRS signal is reduced, corresponding to a negative signal in our setup. In principle the missing emission could be (over-)compensated by Raman emission scattered off  $S_1$  or other states different from  $S_0$ , but also Raman absorption by  $S_1$  is possible, depending on

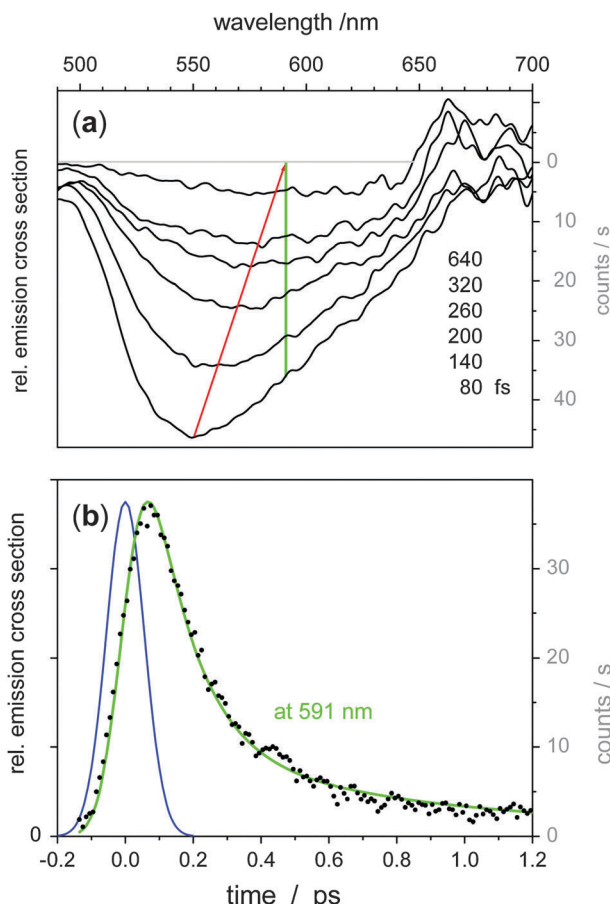


**Fig. 3** (a) Time-resolved fluorescence spectra from broadband upconversion. For comparison, they have been transformed into corresponding spectra for stimulated emission. Scatter from gate harmonics obscures the region around 650 nm. Global analysis reveals a peak shift (red line) of  $1340\text{ cm}^{-1}$  during the decay. (b) Fluorescence intensity at 591 nm (black dots) and corresponding cut through a global fit (green line, see text) together with the instrumental response function (blue).

resonance conditions. The ground-state stimulated Raman spectrum (red) was recorded separately by omitting the actinic pulse. For a decomposition of the signal, the amplitude of the ground-state bleach signal is estimated for every delay time. At spectral positions where the transient signal is dominated by ground-state Raman features, the sharply spiking peaks can be distinguished from the slowly varying background by forming the derivative of the signal. Thus, a scaled ground-state Raman spectrum is subtracted from the transient signal and  $\int (\partial \text{residuum}/\partial\tilde{\nu})^2 d\tilde{\nu}$  calculated. Minimisation gives the optimal residuum (blue line in Fig. 4a),<sup>47,63</sup> to which we subsequently refer as the “induced transient Raman spectrum” for the chosen delay time. The amplitudes of the bleach and induced Raman spectra are shown in panel b as a function of time, together with time constants from multiexponential fits (see ESI†).

The time evolution of the induced Raman spectrum is shown in Fig. 5. For the initial period of  $<0.5$  ps the spectrum has dispersive character and is mainly absorptive. This initial signature decays ultrafast ( $\tau_1 = 90$  fs), close to the time resolution of the experiment. Thereafter Raman emission

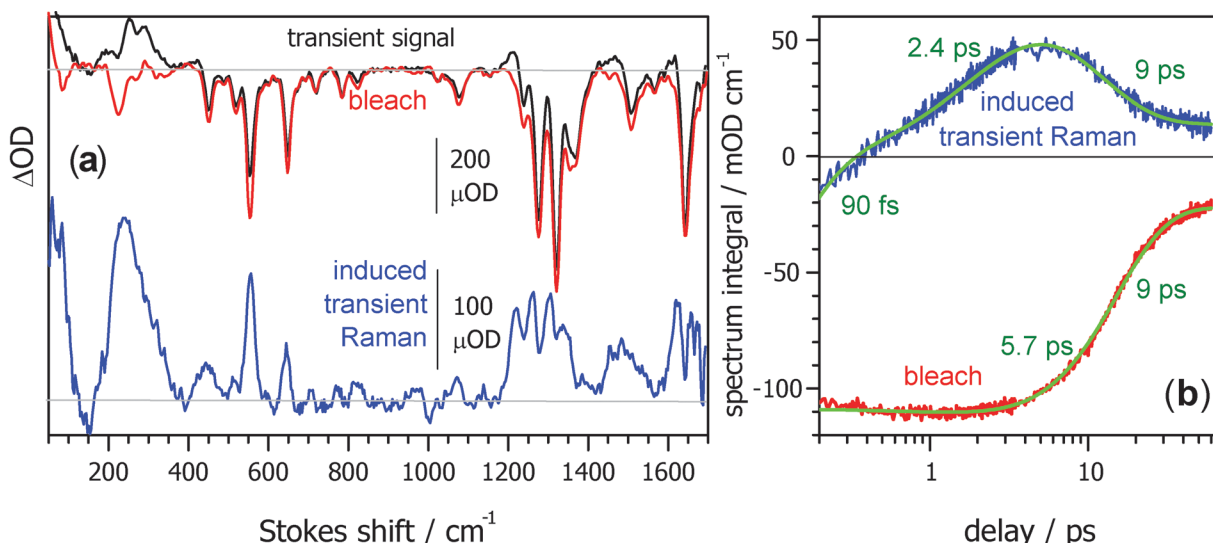


**Fig. 4** (a) Transient Raman signal, for example at 5 ps (black line). The bands are absorptive, generally shown by negative ordinate values.<sup>47</sup> At every delay time the ground-state Raman spectrum (red) is estimated and subtracted. The residuum (blue) represents the induced transient Raman spectrum which is subsequently discussed. (b) Amplitude evolution of the bleach and induced transient Raman spectra (measured by integrals) and multi-exponential fits (green).

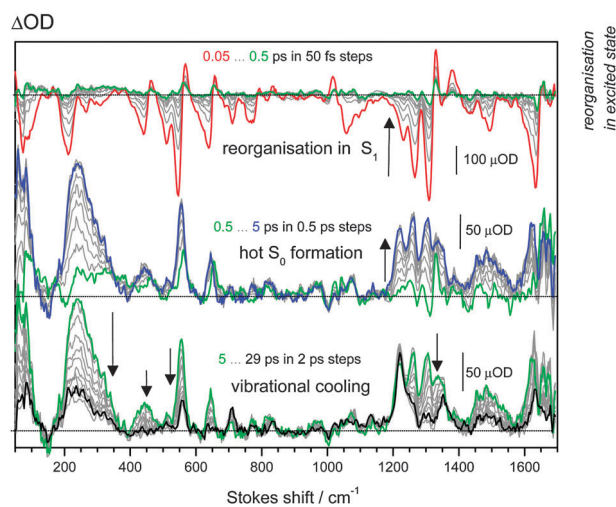


**Fig. 5** Time evolution of the induced transient Raman spectrum after actinic excitation at 482 nm.

grows in, to a peak at 5 ps ( $\tau_2 = 2.4$  ps), and then changes gradually to the “final” induced Raman spectrum at 29 ps, shown as a black line ( $\tau_3 = 9$  ps).

### 3.2 Computational results

**Minimum-energy structures.** The  $S_0$  and  $S_1$  structures of the *trans* isomer of Me-1122-P in methanol ( $\text{minS}_0\text{-trans}$  and  $\text{minS}_1\text{-trans}$  in Fig. 6) were calculated with different functionals. The relative energies of all the stationary points located on  $S_0$  and  $S_1$  PESs are given in Table 1. As in the case of other cyanines, on the PES of the excited state there exists a plateau not far from planar geometries. Here, local optimization (LR-PCM//CAM-B3LYP/6-31G(d)) finds a stationary structure of  $C_2$  symmetry ( $\text{minS}_1\text{-trans}$ ). By contrast, the global minimum  $\text{minS}_1$  exhibits a markedly asymmetric structure with the two dihedral angles  $\phi$  and  $\psi$  close to 0 and  $90^\circ$ , respectively.

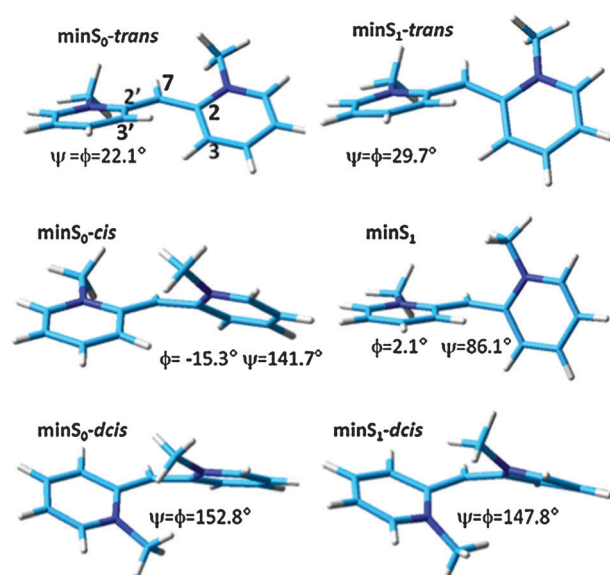


**Fig. 6** Quantum-chemical calculations of 1,1'-dimethyl-2,2'-pyrido-cyanine (Me-P) may be used to characterize the potential energy surface. Shown are the minima of Me-P in methanol at the LR-PCM//CAM-B3LYP/6-31G(d) level of theory. *trans* and *dcis* structures in  $S_0$  and  $S_1$  belong to  $C_2$  symmetry, while  $S_0\text{-cis}$  and the global  $S_1$  minimum ( $\text{minS}_1$ ) belong to  $C_1$ .

Analogous stationary points (see Fig. S2) were found with Et- substituents, confirming that Me-1122-P is a good model for 1122-P.

Whether  $\text{minS}_1\text{-trans}$  corresponds to a true minimum or a transition state is not easy to determine (we find an imaginary frequency  $i348 \text{ cm}^{-1}$  which drops to  $i26 \text{ cm}^{-1}$  for 1122-P). Nonetheless, from a dynamical point of view this is not a major point: on one side we prove in the following that a possible barrier is very low, on the other side even the absence

**Table 1** Energies (eV) of *trans*, *cis*, and *dcis* isomers on  $S_0$  PES optimized in methanol by CAM-B3LYP, and *trans*, *dcis* and min $S_1$  stationary points on  $S_1$  PES optimized in methanol at the LR-PCM//CAM-B3LYP level.  $S_1$  energies in the *neq* regime. *eq* values are reported in italics

Structure	6-31G(d)		6-311+G(2d,2p)	
	$E(S_0)$	$E(S_1)$	$E(S_0)$	$E(S_1)$
min $S_0$ - <i>trans</i>	0.0	3.247	0.0	3.194
min $S_1$ - <i>trans</i>	0.184	3.097	2.885	
min $S_0$ - <i>cis</i>	0.176	3.401	0.181	3.349
min $S_0$ - <i>dcis</i>	0.366	3.527	0.372	3.461
min $S_1$ - <i>dcis</i>	0.831	3.129		
min $S_1$	0.776	2.867		
		2.862		

of a barrier does not imply that there are strong driving forces to leave the quasi-planar  $C_2$  region and reach the global minimum. In the gas phase (see Fig. S3, ESI†), the plateau looks less extended than in solution, suggesting a longer residence time in methanol than in the gas phase.

The global  $S_1$  minimum (min $S_1$ , all positive vibrational frequencies) exhibits partial CT character. Referring to Fig. 6, the molecular left ring is essentially coplanar with the central CH bond ( $\phi = 2.1^\circ$ ). This left ring can be considered as the donor in a partial electron-transfer process to the right moiety, which is oriented perpendicular ( $\psi = 86.1^\circ$ ) while the central CH moiety remains essentially neutral. Mulliken population analysis (SS-PCM/CAM-B3LYP calculations in the *eq* regime) indicates that indeed, the sum of  $S_1$  atomic charges on the left and the right moieties are +0.77 au and +0.19 au, respectively.

The *cis* isomer in the electronic ground state (min $S_0$ -*cis* in Fig. 6) and a *double-cis* (*dcis*) isomer (min $S_0$ -*dcis*) were also optimized. The former will be made responsible for differences in the optical and Raman spectra which remain  $\sim 30$  ps after photoexcitation. The possibility of isomerization around both central bonds was already highlighted in previous papers on NK88 thiacyanine.<sup>24,25</sup>

**Minimum energy  $S_1$  paths (MEP).** MEP in methanol from the FC point to the global  $S_1$  minimum were obtained for a series of fixed values of dihedral  $\psi$ , by optimization of all other internal coordinates on  $S_1$  at the LR-PCM//TD-CAMB3LYP/6-31G(d) level of theory, Fig. 7. We also built a constrained  $C_2$  MEP (where by definition  $\phi = \psi$ , see Fig. 7d). The  $C_2$  path shows a first stationary point at about  $30^\circ$ , corresponding to the min $S_1$ -*trans* structure of Fig. 6, with an energy *ca.* 0.15 eV lower than in the FC point. For larger  $\psi$  the  $C_2$  energy increases and shows some peculiar (though smooth) oscillatory behavior, possibly due to steric hindrances. From min $S_1$ -*trans* an apparently barrierless  $C_1$  path brings the system to the global minimum min $S_1$  at  $\psi \approx 90^\circ$ . Fig. 7d shows the  $\phi$  value for each structure along the MEP. Note that for  $\psi < 25^\circ$ ,  $\phi$  approaches values close to  $90^\circ$ . Those structures correspond to the global minimum symmetric to min $S_1$  where values of  $\psi$  and  $\phi$  are simply interchanged. This is the reason why in Fig. 7a the  $C_1$  path is plotted starting at  $\psi \approx 30^\circ$ . The following picture arises. The system is excited on a plateau of the  $S_1$  PES. As soon as one of the two dihedrals increases,

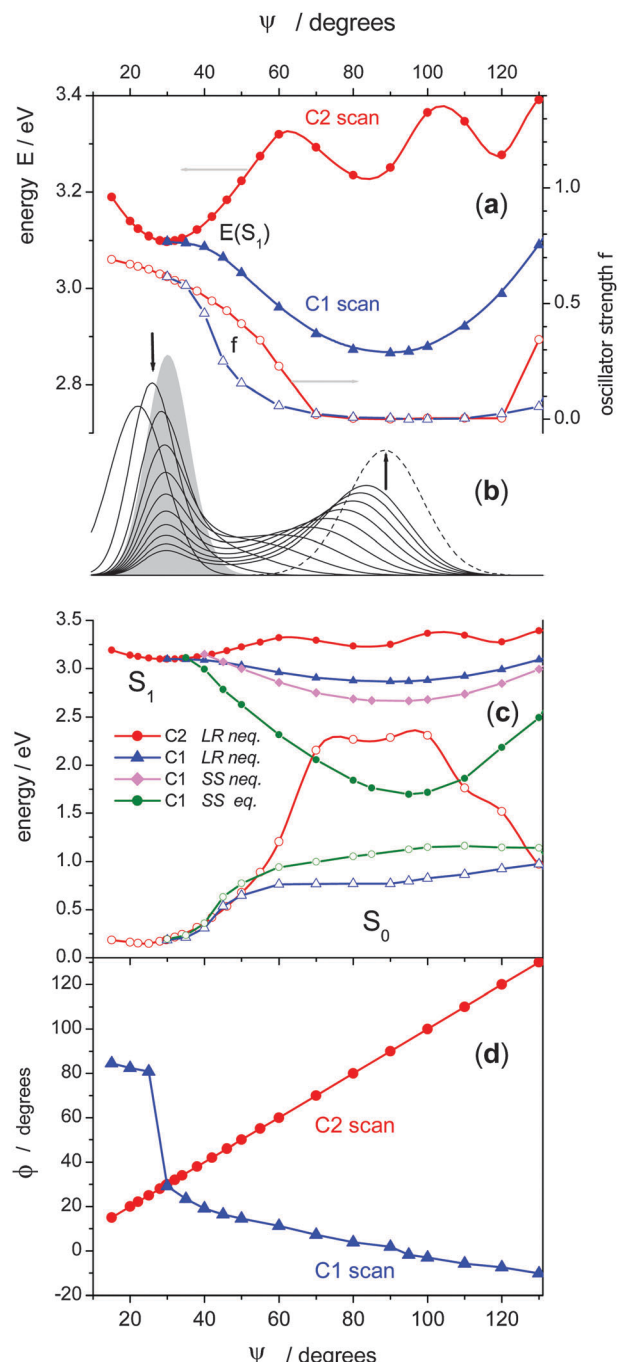


**Fig. 7** Minimum-energy-paths on the  $S_1$  PES, as a function of dihedral  $\psi$ . For comparison with experiments, transition energies should be corrected by  $-0.55$  eV. (a)  $S_1$  energies and  $S_0/S_1$  oscillator strengths (open symbols); the solvent is described at the nonequilibrium LR-PCM level. (b) Distributions calculated for 0, 20, 50, 80 fs after excitation, and then in 30 fs steps to 320 fs. The gray band represents the stationary distribution which would be reached if the  $C_1$  path were absent, and the dashed line the final distribution. Arrows indicate population decay and growth. (c)  $S_0$  and  $S_1$  energies (at the SS and LR level, the latter as in (a)) on a common scale; see text. (d) Associated  $\phi$  values.

moving toward min $S_1$ , the system accesses a region of the PES where min $S_1$ -*trans* lies and  $C_1$  and  $C_2$  paths are isoenergetic, up to  $\psi = \phi \approx 40^\circ$ . Further increase in  $\psi$  or  $\phi$  makes the  $C_2$  path, potentially leading to the *dcis* isomer, too high in energy

and hence inaccessible, while the  $C_1$  path, toward the *cis* isomer, decreases the potential energy while increasing the CT character of the electronic state, finally leading to  $\text{minS}_1$ . The  $\phi$  values for  $\psi < 25^\circ$  suggest however the possibility that part of the photoexcited FC wavepacket (see also the extension of the initial distribution in Fig. 7b) does not reach  $\text{minS}_1$ -*trans* and directly moves toward  $\text{minS}_1$  (or its  $\psi/\phi$  symmetric structure). Only dynamical simulations allow, in principle, to estimate the relative yields of the two paths; however they would be so critically dependent on the topology of the PES in the region encompassing FC and  $\text{minS}_1$ -*trans* structures that no conclusive answer is expected from calculations alone. A CI is still far from the global minimum  $\text{minS}_1$ ; in fact at this geometry the  $S_1/S_0$  energy gap is still  $> 2.0$  eV (*cf.* Fig. 7c).

The  $S_1/S_0$  oscillator strength (empty circles in Fig. 7a) is predicted to decrease and vanish when the  $\sim 90^\circ$   $\text{minS}_1$  structure is approached. Only very weak fluorescence or SE should occur after the system has left the region around  $\psi = \phi = 30^\circ$ .

Refinement of the LR-PCM PES at the SS-PCM//CAM-B3LYP/6-31G(d) level produces the additional curves in Fig. 7c. Just after excitation the solvent can be considered still in equilibrium with  $S_0$  while it is in non-equilibrium with  $S_1$  (*magenta solid squares*). At longer times (assuming that the system remains in  $S_1$ ) the solvent equilibrates with the excited state (*green solid circles*), whereas it reaches a nonequilibrium situation with the ground state (*green empty circles*). At intermediate times the system should exhibit a behavior between these limits. As expected, at this more refined computational level the  $S_1/S_0$  energy gap is reduced. The gap shrinks to less than 0.5 eV in the equilibrium regime of solvation for  $S_1$ , where the whole solvent polarization is equilibrated with the excited-state charge density, suggesting that solvent relaxation plays an important role in making accessible the  $S_1/S_0$  CI.

**Absorption and emission spectra of the *trans* isomer.** The vibrationally resolved absorption and emission spectra of *trans* Me-1122-P in methanol (gray lines in Fig. 8a) were computed at the CAM-B3LYP level of theory. The harmonic approximation includes frequency changes and Duschinsky mixings for all the 84 normal modes (AH model).<sup>64</sup> Following absorption, the wavepacket generated in  $S_1$  is assumed to roam on the  $C_2$  plateau around the  $\text{minS}_1$ -*trans* structure long enough so that other regions of configuration space do not contribute significantly to the spectrum. For technical reasons (see ESI†) the spectra have been computed by imposing to  $\text{minS}_1$ -*trans* the same  $\phi = \psi = 22.1^\circ$  of the ground state minimum. All calculated spectra have been shifted by 0.55 eV to match with experimental results, as discussed further below. The peak at about  $400\text{ cm}^{-1}$  from the origin is due to a progression along mode 18, a ring deformation (ESI†). The shoulder at about  $1150\text{ cm}^{-1}$  is a multimode effect arising from the contribution of many progressions, the dominant being that along mode 52, a combination of ring stretches and hydrogen in-plane bendings (ESI†). The latter is also responsible for a strong band in the resonance Raman spectra (see below).

**Comparison of *trans*, *cis* and *deis* absorption spectra.** Induced absorption which remains after internal conversion and

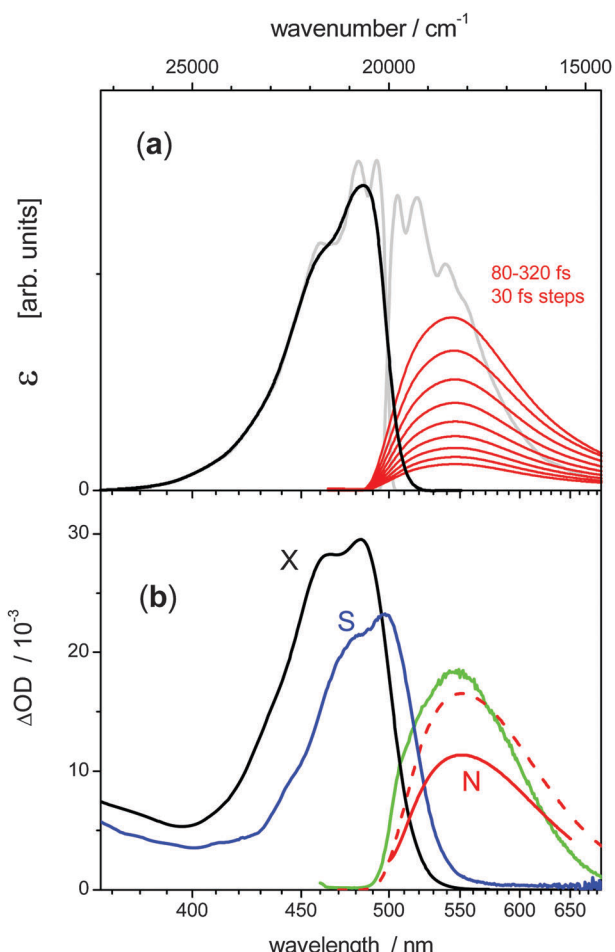


**Fig. 8** (a) Calculated absorption and stimulated-emission spectra of Me-P in methanol for the *trans*-isomer (gray lines; see text). Convolution with spatial distributions  $P_i(\psi)$  and oscillator strengths (Fig. 7a and b) gives the time-dependent spectra for stimulated emission (red). Similarly the absorption spectrum is obtained (black). For comparison with (b) all calculated envelopes have been red-shifted by 0.55 eV. Delay times of 80–320 fs allow direct comparison with Fig. 2a and e. (b) Experimental spectra of 1122-P: *trans* (X) and *cis* (S) absorption bands in methanol. The latter was extracted from the latest (60 ps) transient spectrum which is their difference. The stimulated emission spectrum at time-zero (N, deconvoluted from the data in Fig. 3a) is consistent with the observed bleach at 80 fs. Relative amplitudes were estimated by imposing that the sum of absorption (as bleach) and SE should match the initial TA spectrum. This procedure neglects ESA and therefore the true SE amplitude could be higher. If instead the calculated ratio of oscillator strengths applies, then the red-dashed curve would be observed. Green: stationary fluorescence as in Fig. 1, but re-expressed as stimulated emission.

cooling (for example at 50 ps, blue line in Fig. 2d) will later be assigned to the *cis* isomer. It is not possible to compare the absorption spectra of all the isomers uniformly with the AH approach, since for the *cis* isomer,  $S_1$  geometry optimization leads directly to  $\text{minS}_1$  and does not provide a representative pseudo-stationary point. As a consequence, for uniformity we resorted to the less accurate VG approximation. Results are collected in Table 2 (the computed spectra are given in Fig. S4 of the ESI†). Independent of the functional, basis set, and solvation regime adopted, we find that the vertical transition

**Table 2** *trans*, *cis* and *dcis* vertical excitation energies (eV) in *neq* and *eq* regimes

Structure	CAM-B3LYP															
	6-31G(d)				6-311+G(2d,2p)											
Structure	LR	neq	LR	eq	SS	neq	SS	eq	LR	neq	LR	eq	SS	neq	SS	eq
minS <sub>0</sub> -	3.247	3.019	3.353	3.335	3.194	2.962	3.290	3.267								
<i>trans</i>	(0.76)	(0.96)	(0.65)	(0.64)	(0.77)	(1.00)	(0.65)	(0.65)								
minS <sub>0</sub> - <i>cis</i>	3.225	3.018	3.317	3.286	3.168	2.958	3.248	3.194	(0.66)	(0.85)	(0.56)	(0.55)	(0.67)	(0.88)	(0.55)	(0.53)
minS <sub>0</sub> - <i>dcis</i>	3.161	2.966	3.261	3.240	3.088	2.892	3.179	3.153	(0.593)	(0.79)	(0.49)	(0.49)	(0.58)	(0.80)	(0.48)	(0.47)

Oscillator strength in parentheses. Notice in ESI also B3LYP results are reported.

energy and the oscillator strength increase in the order *dcis* < *cis* < *trans*. Since we are dealing with an absorption process, *neq* data are more directly comparable with experiment than *eq* ones. Therefore, according to our best estimate (SS-PCM//CAM-B3LYP/6-311+G(2d,2p) results) the difference in absorption maxima between *cis* and *trans* species is 0.04 eV (320 cm<sup>-1</sup>) with a ratio of oscillator strengths 0.85. Notice from inspection of Table 2 that extension of the basis introduces a slight red-shift of the excitation energies that is almost constant for the three different isomer structures, further supporting the reliability of the CAM-B3LYP/6-31G(d) level of theory adopted for more extensive explorations of the PES.

Vibrational resonance Raman spectra were computed for the three different isomers (see ESI† for a detailed description) at different levels of theory, with the AH approach,<sup>58</sup> and within the simpler STD approach (VG).<sup>62</sup> VG and AH results are entered as red and green lines, respectively, in Fig. 10 which will be discussed below.

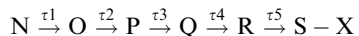
#### 4. Assignments: mapping experimental transients to regions of the minimum energy path

##### 4.1 Excited-state dynamics

Kinetic analysis of transient absorption (Fig. 2) must cope with rich dynamics which is hidden in small spectral change. The photoisomerisation has been modeled as spectral diffusion which is inherently nonexponential.<sup>7,19,65–67</sup> But for any given noise level, a multiexponential description may be substituted which can then be cast into a kinetic sequence of virtual states. The (virtual) species-associated-spectra (SAS<sub>i</sub>) accentuate the characteristic spectral features which, in smooth transition, blend into the continuous process.

As already mentioned in the results section, 5 linearly independent spectra are involved and therefore, four exponential functions and one Heaviside function are needed in our case. One of the four exponential time constants is sub-ps (0.21 ps) while the others are 3.7, 4.2, and 15.7 ps. Turning for a moment to the FLUPS data (Fig. 3) we find an average fluorescence decay time of ~0.2 ps, close to the fastest time constant for TA. But the FLUPS data show clearly that the sub-ps decay is bi-exponential ( $\tau_1 = 0.13$  ps and  $\tau_2 = 0.88$  ps). In order to include this information into our kinetic analysis of

TA, we therefore add another time constant and assign the same value (0.13 ps) to the fastest component. In summary, the process under investigation is described by the following kinetic scheme



(here X refers to the loss of reactant population due to the photoisomerisation), and the optimal time constants are  $\tau_1 = 0.13$  ps,  $\tau_2 = 0.88$  ps,  $\tau_3 = 3.7$  ps,  $\tau_4 = 4.2$  ps,  $\tau_5 = 15.7$  ps. The SAS are shown in Fig. 9. Later we will see that the first three indicate transients on the S<sub>1</sub> PES, so that they are marked by an asterisk, N\* → O\* → P\* → Q → R → S-X. Slightly different rate constants can give an equally good fit, but the corresponding SAS are not substantially different.

Immediately after photoexcitation, the evolution from the FC geometry to the minS<sub>1</sub>-*trans* structure is predicted (below) to be unresolvably fast for our experiments. This permits us to identify the initial empirical state N\* with minS<sub>1</sub>-*trans*. The latter still carries significant oscillator strength and should be responsible for most of the emission, especially at early times. Note however that the computed absorption and emission spectra, with minS<sub>1</sub>-*trans* as reference geometry in S<sub>1</sub>, are more structured than the experimental absorption of 1122-P and than the SE band at time zero (from fluorescence, red lines in Fig. 8b). Indeed the measured absorption spectrum is partially resolved, while the experimental SE spectrum is totally unstructured. The predicted red shoulder is not observed at 80 fs; instead a broad unstructured SE band extends to lower energies, centered about 1000 cm<sup>-1</sup> below the position predicted at  $t = 0$ . This is explained by the fact that, while emitting, the molecule undergoes photoisomerization.

**Simulation of the spectral evolution.** Diffusion and drift along the S<sub>1</sub> reaction path are calculated next, starting with the distribution  $P_0(\psi)$  of the electronic ground state. As potential-energy curve  $V_1(\psi)$  we take the C<sub>2</sub> path from the FC point to minS<sub>1</sub>-*trans* and then continue along the C<sub>1</sub> path to minS<sub>1</sub>. In other words, the decay channel that removes the C<sub>2</sub> symmetry right after the excitation, without passing through minS<sub>1</sub>-*trans*, is assumed to be of minor importance. Let  $V_0(\psi)$  denote the potential energy in the electronic ground state as seen from the path sketched above (all relevant potential-energy curves are parametrized in the ESI†). The time-dependent distribution  $P_t$  is governed by the Smoluchowski equation<sup>68</sup>

$$\dot{P}_t = -\mathfrak{S}P_t$$

having the operator

$$\mathfrak{S} = -\frac{1}{\gamma I} \left\{ k_B T \frac{\partial^2}{\partial \psi^2} + \left( \frac{\partial V}{\partial \psi} \right) \frac{\partial}{\partial \psi} + \left( \frac{\partial^2 V}{\partial \psi^2} \right) \right\}$$

Here  $\gamma$  is the friction constant (the only adjustable parameter of the present analysis) and  $I$  the moment-of-inertia (139 amu Å<sup>2</sup> from the minS<sub>1</sub>-*trans* structure;  $\psi$  is in radians). Furthermore  $T = 300$  K is assumed to be maintained during the evolution. Snapshots of  $P_t(\psi)$  are shown in Fig. 7b. Using the curves for  $V_1 - V_0$  and oscillator strengths, we arrive at spectral distributions for the electronic transition energy S<sub>1</sub> → S<sub>0</sub>. These distributions are then convoluted with the

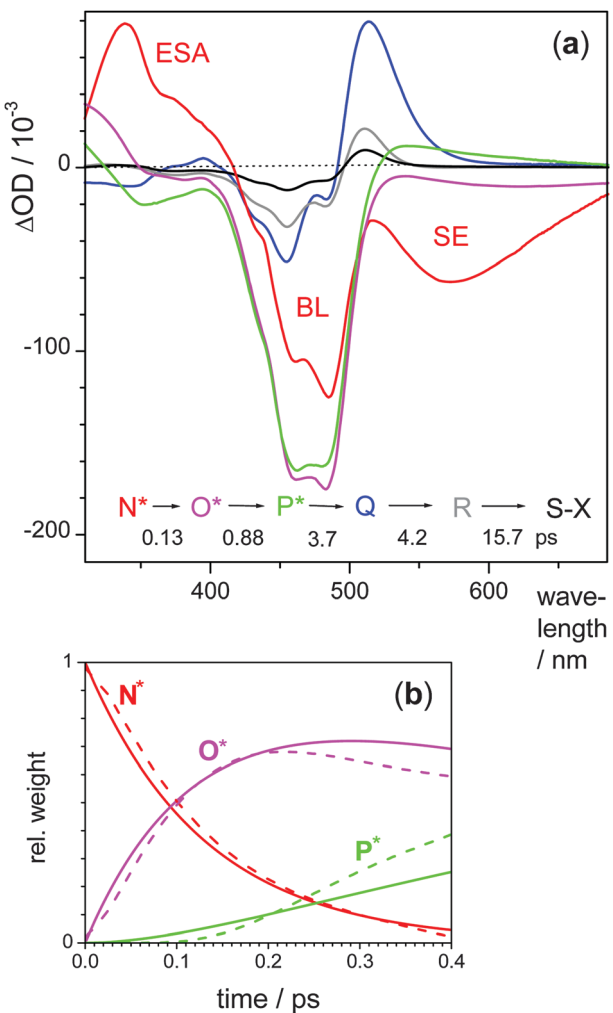


**Fig. 9** (a) State-associated transient absorption spectra, from a kinetic analysis of the data in Fig. 2a–d. The fluorescence dynamics observed separately (Fig. 3) contributed the first two time constants, allowing a differentiated view of the photoreaction before 1 ps. The initial SE band is quickly reduced upon transition to virtual state  $O^*$ . It then gives way to weak broad ESA from state  $P^*$ , which must be assigned to the perpendicular geometry before internal conversion (see text). The long-lived final spectrum is assigned to the *cis* isomer  $S$  together with the corresponding *trans* bleach,  $-X$ . (b) Empirical weights of the first three “species” at early time (*solid*). They are compared to calculated population fractions (*dashed lines*, see text) of the evolving distribution  $P_t(\psi)$  in the  $S_1$  state.

vibronic lineshape for emission. After multiplication with the frequency, the corresponding  $SE(t)$  bands are obtained (red lines in Fig. 8a). They compare well with the experimental counterparts from FLUPS (Fig. 3a). We find that  $\gamma = 4.42 \text{ ps}^{-1}$  describes best the observed decay of the emission spectrum at 591 nm, for example. Also a red-shift is predicted over the first picosecond, albeit less than the  $1340 \text{ cm}^{-1}$  which is observed experimentally. Comparison of  $neq$  and  $eq$  reaction paths in Fig. 7b suggests that the discrepancy is due to the neglect of solvation dynamics.

The simulated ground-state absorption band (black line in Fig. 8a) is derived simply by convoluting with the spectral distribution  $V_1 - V_0$ , pertaining to stationary  $P_0(\psi)$  in  $S_0$ .

Calculated transition energies are systematically reduced by 0.55 eV to match the experimental absorption peak. This error is larger than typical TD-DFT errors for other classes of chromophores, but not surprising when dealing with a cyanine dye.<sup>50</sup> Very recent results<sup>51</sup> indicate that such error might be reduced with large aug-cc-pVTZ basis sets and new functionals like those of the Minnesota family. In ESI† we show that the error is already reduced by  $\sim 0.2$  eV at the B3LYP/6-31G(d) level and a further reduction of  $\sim 0.1$  eV would be gained by adopting the larger 6-311+G(2d,2p) basis set (unfeasible for extensive exploration of the MEP). However, for a reliable simulation of the dynamics of the photoexcited distribution it is necessary to describe the whole  $S_1$  MEP with comparable accuracy; this can be obtained by CAM-B3LYP while the performance of B3LYP is known to deteriorate when the excited-state assumes a CT character (for example at min $S_1$  the  $S_1 - S_0$  energy gap is predicted to be reduced by more than 0.6 eV compared to CAM-B3LYP results and therefore the B3LYP MEP is much steeper than predicted by CAM-B3LYP).

Focusing on the absorption spectrum, notwithstanding the rather large error on the transition energy, CAM-B3LYP provides a description of the  $S_1$  state similar to B3LYP; moreover the next (weak) bright state is computed 1 eV to the blue. Therefore even at the CAM-B3LYP level it is safe to assign the experimental spectrum to  $S_1 \leftarrow S_0$  only and to apply a shift on the computed spectrum for comparing the spectral shapes. The agreement with the experimental lineshape further strengthens the assignment. Specifically, in agreement with experiment, the calculated absorption spectrum shows a shoulder  $\approx 1000 - 1100 \text{ cm}^{-1}$  blue-shifted from the main peak. The experimental shoulder is therefore assigned to multimode effects, and in particular to progressions in modes of  $S_1$  that project onto the 52 mode of  $S_0$ . The feature reflects the fact that the min $S_0$ -*trans* and min $S_1$ -*trans* structures are quite displaced along this  $S_0$  mode. Even larger displacements are seen along mode 18 ( $574 \text{ cm}^{-1}$  in  $S_1$ , not strongly affected by Duschinsky mixing) but inhomogeneous broadening washes out the narrowly-spaced progression along this mode.

The empirical amplitudes  $a(t)$  of  $N^*$ ,  $O^*$ ,  $P^*$ , their rise and fall (solid lines in Fig. 9b), are simulated with the same concept. For this purpose the spectral states must be mapped onto different parts of the excited state PES. We find that the decay curve  $a_N(t)$  is nicely mimicked by the integral  $\int_{\psi_A}^{\psi_B} P_t(\psi) d\psi$  for the range  $\psi \leq 37.5^\circ$  (dashed red line). That range contains the hypothetical distribution in the min $S_1$ -*trans* valley if  $C_2$  symmetry, *i.e.*  $\phi = \psi$ , was maintained (95% of the gray band in Fig. 7b). Interestingly, Fig. 7b shows that the evolution of  $P_t(\psi)$  looks as if the early Gaussian sits on a shelf around min $S_1$ -*trans* and simply decays, with the population accumulating in min $S_1$ . The agreement between the simulated and experimental amplitude confirms our assignment  $N^* \equiv \text{min}S_1\text{-}trans$ .

In the final part of the  $S_1$  path, the fraction of molecules with  $\psi \geq 86^\circ$ , *i.e.* in the min $S_1$  region, behaves like empirical  $a_P(t)$  during the first half picosecond (green lines in Fig. 9b). Therefore  $P^*$  can be identified with the excited state in the perpendicular arrangement of the two pyrido moieties.

Full bleach and only faint  $S_n \leftarrow S_1$  absorption to the red (*cf.* Fig. 9a) constitute a kind of spectral limbo for this “phantom state”, named in analogy to excited stilbene.<sup>69,70</sup> Remember that  $P^*$  was uncovered by TA, and it has been identified only when the kinetics obtained by FLUPS was introduced into the analysis. The amplitude  $a_P(t)$  is maximal at 1.8 ps because of the third rate process of our series, with  $\tau_3 = 3.7$  ps. That process corresponds to internal conversion as shown later.

Having mapped the  $N^*$  and  $P^*$  states to regions of the MEP, we find that the simulated population fraction in the intermediate range  $37.5^\circ \leq \psi \leq 86^\circ$  reaches its maximum around 0.3 ps like the empirical amplitude of  $O^*$ . The oscillator strength for emission from  $O^*$  ( $\approx 0.05$ ) and band center (650 nm) is estimated, from measurements, *via* the SAS. The situation corresponds to a mean torsional angle  $\psi \approx 50^\circ$  when Fig. 7a is considered. Polar solvation by methanol could shift the emission further to the red. Typically 40% of the full dynamic Stokes shift in methanol is traversed in the first 0.9 ps.<sup>40</sup> For the range around  $\psi \approx 50^\circ$ , emission at 780 nm is expected by that time. Unfortunately our TA did not extend to this region. But the  $P_t$  simulations suggest that loss of oscillator strength (upon further torsion) is responsible for the disappearance of  $O^*$  (having 0.88 ps decay time). In passing we note that red-edge excitation is expected to shift the initial emission from  $N^*$  towards  $O^*$ . Turning to experiments, the SE in Fig. 2e was created by red-edge excitation (at 495 nm, *cf.* Fig. 1), and indeed, the initial emission appears significantly red-shifted with respect to the one observed with excitation at 442 nm.

## 4.2 Ground-state dynamics

**Evolution of electronic spectra.** The electronic ground state is best unraveled from the end. After 50 ps (blue line in Fig. 2d) no further development is seen, suggesting that the molecular system is equilibrated internally and with the solvent. The spectrum ( $=SAS_{S-X}$ ) has the dispersive shape which is characteristic of reactant bleach ( $-X$ ) together with product absorption ( $S$ ). The natural assignment for  $S$  is the product of the isomerization, *i.e.* the *cis* isomer. In agreement, the absorption band of the *cis* isomer is computed slightly red-shifted from the *trans* one and less intense. Assuming the calculated ratio of oscillator strengths for absorption, we find the absorption spectrum of the *cis* isomer which is shown in Fig. 8b. The corresponding reactant bleach can now be compared to the initial bleach, and in this way we estimate a quantum yield of  $\approx 17\%$  for *trans–cis* isomerisation.

The preceding  $SAS_R$  has a red lobe with identical shape but  $2.2\times$  higher amplitude. The 15.7 ps process  $R \rightarrow S$  could indicate fractional *cis*  $\rightarrow$  *trans* isomerisation in the ground state, or cooling, or both. The absorption lobe at 525 nm is strongest (compared to the remaining bleach) around 5 ps. It is also significantly broader compared to the later stages.

**Evolution of Raman spectra.** As experimental evidence we have (i) the ground-state Raman spectrum (*red line* in Fig. 4a) and its relative bleach in the transient spectra (lower part of Fig. 4b), (ii) the remaining part, called “induced transient” (upper part). The Raman bleach stays maximal until about 3 ps,

like the optical bleach which was discussed in the previous section. Then it recovers with  $\sim 9$  ps characteristic time to an offset of *ca.* 20%. The spectral development is carried by the induced transient signal (not by the bleached Raman spectrum) which therefore was subjected to a global multi-exponential analysis. Three time constants are necessary to describe the evolution: 90 fs, 2.4 ps, and 9 ps. When these are arranged into a series of virtual states as before, we find the associated Raman spectra which are shown in Fig. 10. The initial Raman spectrum has dispersive character and is mainly absorptive, as already mentioned. The complicated structure is a consequence of multiple resonance conditions<sup>63</sup> which, unfortunately, prevent further analysis.

An intermediate Raman spectrum rises to maximum weight at 5 ps, like the replenished ground state  $Q$  (from kinetic analysis of TA) just after internal conversion, to which it is now assigned. Note that the Raman pump wavelength (520 nm) was tuned to the induced absorption lobe of  $Q$  (see Fig. 9a).

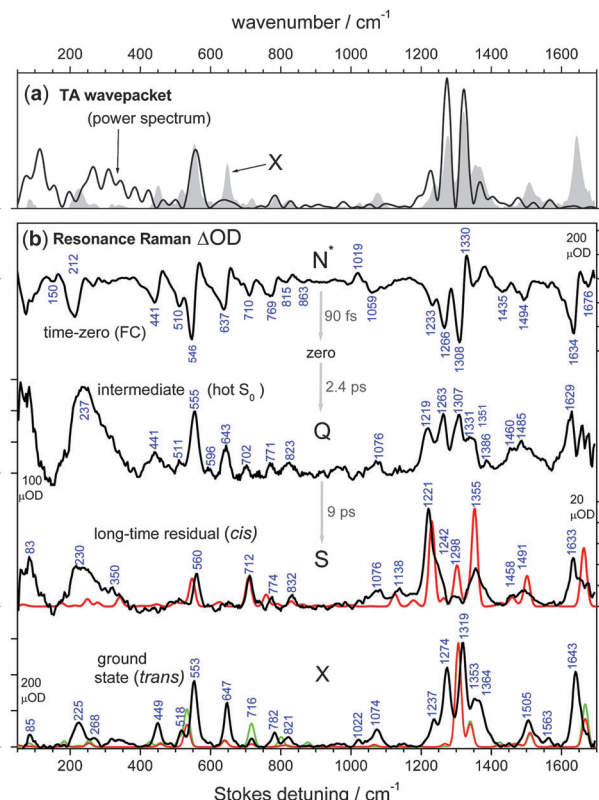


**Fig. 10** (a) Wavepacket power spectrum (*black line*), from monitoring transient absorption in the emission region. (b) Experimental species-associated Raman spectra (*black lines*), from global analysis of the FSRS evolution (Fig. 5) with time constants taken from the behavior of the spectral integrals (Fig. 4b). The time-zero spectrum  $N^*$  disappears with 90 fs time constant. Then an intermediate spectrum  $Q$ , attributed to a hot  $S_0$  state, rises with 2.4 ps. It decays with 9 ps to a long-time residual  $S$  which can be assigned to the *cis*-conformer, having a marker band at  $1221\text{ cm}^{-1}$ . For comparison, the ground-state Raman spectrum  $X$  of the original *trans* form is also shown, and repeated in (a) as *gray bands*. Computed Raman spectra of *trans* and *cis* isomers of Me-P, with  $S_0 \rightarrow S_1$  resonance excitation, are shown by red (VG model) and green (AH) lines. The CAM-B3LYP/6-31G\* level of theory was used, and harmonic frequencies have been scaled by 0.96.

Features at  $1229\text{ cm}^{-1}$  and in the low-frequency region around  $240\text{ cm}^{-1}$  are typical for the *cis* product. Other bands resemble a shifted *trans* spectrum, which seem to be partly overlayed by dispersive lineshapes at the positions of the *trans* Raman spectrum (see for example the region around  $1640\text{ cm}^{-1}$ ). Since the induced Raman spectra discussed here have the *trans*-cyanine contribution subtracted, dispersive bands at the corresponding positions can be understood as a spectral shift of *trans* bands. Disappearance of such features can be explained by spectral relaxation due to vibrational cooling.

The final induced Raman spectrum ( $S$ ) should belong to the *cis* isomer. Although the limited accuracy of the VG model (see Fig. S5–S9 in ESI† for details) and the similarity of the computed vRR spectra of the different isomers do not allow unambiguous conclusions, our assignment is supported by two qualitative features: (i) in the  $1200$ – $1400\text{ cm}^{-1}$  region the calculated *cis* isomer has a strong band on the low-energy wing of the *trans* peaks, (ii) in the  $500$ – $750\text{ cm}^{-1}$  region it shows two peaks of equal intensity, at variance with the *trans* species which has only a single strong peak at lower energy and a weaker peak at larger detuning (see Fig. S10 in ESI†). Notice that from data in Fig. SI9–SI10 (ESI†) it is predicted that the *dcis* spectrum should be very similar to *cis* one, with a partial weakening of some secondary bands.

The complementary *trans* part at late time is given by the offset ( $-X$ ) which was mentioned above. The main observed Raman features of the *trans* isomer are reproduced by our VG calculations. The agreement improves with the AH model (see Fig. 10a and Fig. S5), especially in the region  $500$ – $750\text{ cm}^{-1}$ , but unfortunately this model is not applicable to the *cis* isomers.

## 5. Discussion

In the preceding section we identified transient states of 1122-P and assigned them to regions along a calculated reaction path. Time-dependent populations for the different virtual species were estimated from the PES, obtained by PCM/TD-CAM-B3LYP calculations; they were also extracted from joint FLUPS and TA measurements. The agreement between both measurements indicates that our calculations provide a fairly reliable basis for discussing the photoisomerization process. This concerns primarily the motion along the reaction coordinate, but also vibrations of associated “spectator” coordinates. The latter can potentially be identified as shifting bands in the transient FRSR spectra. But in the present case, unfortunately, the analysis is frustrated by an observed crowdedness and calculated quasi-degeneracy of Raman bands for the *trans* and *cis* isomers.

### $\text{FC} \rightarrow \text{N}^*$ transition

According to our calculations  $\text{N}^* \equiv \text{minS}_1\text{-}trans$  is reached from  $\text{minS}_0\text{-}trans$  (the FC state) by symmetric motion, like mode 52. Displacements involve mainly the  $\text{C}_2\text{--C}_7$ ,  $\text{C}_2\text{--N}$  and  $\text{C}_2\text{--C}_3$  bonds (and the symmetric counterparts in the left ring) which change by  $+0.02$ ,  $+0.02$  and  $-0.02\text{ \AA}$ , respectively. Simultaneously the  $\text{C}_2\text{--C}_7\text{--C}_2$  bond angle decreases by  $3^\circ$  because steric hindrance is reduced. We argued above that this early reorganisation is not resolved in our measurements.

### $\text{N}^* \rightarrow \text{O}^*$ and $\text{O}^* \rightarrow \text{P}^*$ transitions

The subsequent path from  $\text{minS}_1\text{-}trans$  towards the  $\text{minS}_1$  region requires the activation of symmetry-breaking modes. Already at  $\psi = 45^\circ$  the minimum energy structure on the  $\text{C}_1$  path shows a marked asymmetry, the  $\text{C}_2\text{--C}_7$  bond being  $0.05\text{ \AA}$  shorter than the  $\text{C}_2\text{--C}_7$  bond. These asymmetric modes are not accelerated directly by the photoexcitation, and it is therefore reasonable that a finite time is needed to pump energy along them. The observed  $0.13\text{ ps}$  time constant (decay of  $\text{N}^*$ ) probably reflects this part of intramolecular vibrational redistribution.

The SE bands in  $\text{SAS}_N$  and  $\text{SAS}_O$  correspond qualitatively to the fluorescence bands observed by the FLUPS experiments (Fig. 3a, Fig. S1 (ESI†)). The BL appears to increase in going from  $\text{N}^*$  to  $\text{O}^*$ , but this is an artifact of the multiexponential description at early time, where the “population” signal partly overlaps with the instantaneous signal due to electronic coherence. In reality the BL stays constant for an induction period, as can be seen in conjunction with the relative weights in Fig. 9b.

Wavepacket motion is induced on the excited state by the femtosecond pump pulse, and can be captured as oscillations of transient absorption by the highly time-resolved measurements. The Fourier transform of the oscillations of TA over the first  $1.6\text{ ps}$  is shown in Fig. 10a. Since we probe to the red of the ground-state bleach, only transitions from the excited state (mainly  $\text{S}_1 \rightarrow \text{S}_0$  stimulated emission) are resonant and dominate the signal. Time-domain Raman spectroscopy provides thus an alternative view on the  $\text{S}_1$  vibrational manifold, which is not obscured by the complex lineshapes found in FSRS. According to our previous analysis, the nuclear distribution runs in the  $\text{S}_1$  state exploring a region of the PES intermediate between  $\text{minS}_1\text{-}trans$  and  $\text{minS}_1$ , and the strongest contributions are expected from the  $\text{N}^*$  virtual state (see below). Band positions and intensities resemble those of the ground-state Raman spectrum ( $X$ ). The spectrum deviates, for example, for the  $1237\text{ cm}^{-1}$  band, which is downshifted to  $1227\text{ cm}^{-1}$  in the  $\text{S}_1$  state.

The assignment of Raman bands gives rise to interesting speculations on the different symmetric/asymmetric nature of the active vibrations in *trans* and *cis* isomers. A detailed discussion is given in the ESI† for the interested reader.

*Solvent effects* may also cause a retardation in removing symmetry, *i.e.* in abandoning the  $\text{minS}_1\text{-}trans$  region. Such motion is accompanied by a rise of  $\text{S}_1$  CT character, *i.e.* with significant rearrangement of charge density. More specifically, SS-PCM calculations predict that while at  $\text{minS}_1\text{-}trans$  the  $\text{S}_1$  electric dipole is  $2.6$  Debye and mainly oriented along the symmetry axis, for the structure at  $\psi = 45^\circ$  it is  $5$  Debye, and its strongest component is now directed toward the left ring (Fig. 6), *i.e.* the one bearing most of the positive charge. It is therefore clear that a polar solvent must rearrange to facilitate the motion along the path away from the  $\text{minS}_1\text{-}trans$  region, and this will require a finite time.

*Some general methodological considerations* should be addressed at last. To what extent can a static exploration of the reacting PES, based on local harmonic expansions and combined with time-independent but fully quantum description

of the spectroscopic signals, rationalize the experimental measurements on a prototypical photoisomerization?

The answer is multifaceted but, in short, encouraging because (i) reproduction of the two-peaked absorption and broad emission bands at 80 fs picks out  $\text{minS}_1\text{-trans}$  as the most representative structure immediately after excitation, (ii) simulations of fast loss and emission shift during the first picosecond support the calculated properties of the minimum-energy path in  $S_1$ , (iii) agreement between experimental transients and those computed from drift and diffusion motion along the torsion allows us to identify the spectroscopic signatures of perpendicular phantom state  $P^*$ , (iv) prediction of the *cis* absorption spectrum permitted us to single out its contribution in the long-time TA residuum, and (v) the simulation of the vibrational RR spectra of the *cis* and *trans* species allowed us to recognize features of the hot precursors at early time ( $Q$ ) and to follow their evolution in FSRS transients. All of these findings have a vibronic origin and are therefore connected with the quantum nature of nuclear motion. Better measurements may distinguish the rates by which the hot *trans* and *cis* isomers are created upon internal conversion.

But failures of the computational predictions are instructive as well. The vibrational structure of the absorption band was described only qualitatively, and the emission oscillator strength at 80 fs was predicted significantly higher (0.62) than what observed (0.43). The discrepancy could come from the functional and/or the basis set used in electronic calculations, or alternatively, from an omission of ESA. Nothing can be said about the times of internal conversion with the current theoretical approach, even if our results suggest that dynamical

solvent effects should be taken into account. Finally, the present minimum-path exploration did not allow the individuation of additional stationary points, or even structures in which the system can remain temporarily trapped for purely dynamical reasons, which would be candidates for the empirical  $Q$  and  $R$  species. More generally, we have no information on the spread of the evolving distribution in all the nuclear coordinates (which may cause broadening of the signals but also more complicated phenomena). This means that it is not even possible to state if  $P^*$ ,  $Q$ ,  $R$  species should be associated with well-defined structures, or with a variety of structures featuring some common properties (e.g.  $\psi$  torsion in a given interval).

## 6. Conclusion

The photoisomerisation of 1,1'-diethyl-2,2'-pyridocyanine in methanol was experimentally monitored by the combination of transient absorption, broadband fluorescence upconversion, and stimulated Raman scattering techniques. The amount and accuracy of spectro-temporal data are unsurpassed for any cyanine, according to our knowledge. Observations are summarized on the right side of Fig. 11. They were cast into empirical states  $N^* \rightarrow O^* \rightarrow \dots S, -X$  with associated spectra, connected by rate processes. This is the smallest number of states that can describe the diffusive dynamics adequately. In addition, a Raman-type spectrum was obtained from initial wavepackets, as seen by transient absorption. Calculated structures and corresponding potential energies are indicated to the left.

Following photoexcitation the system moves unresolvedly fast toward the  $\text{minS}_1\text{-trans}$  region ( $N^*$ ), undergoing small

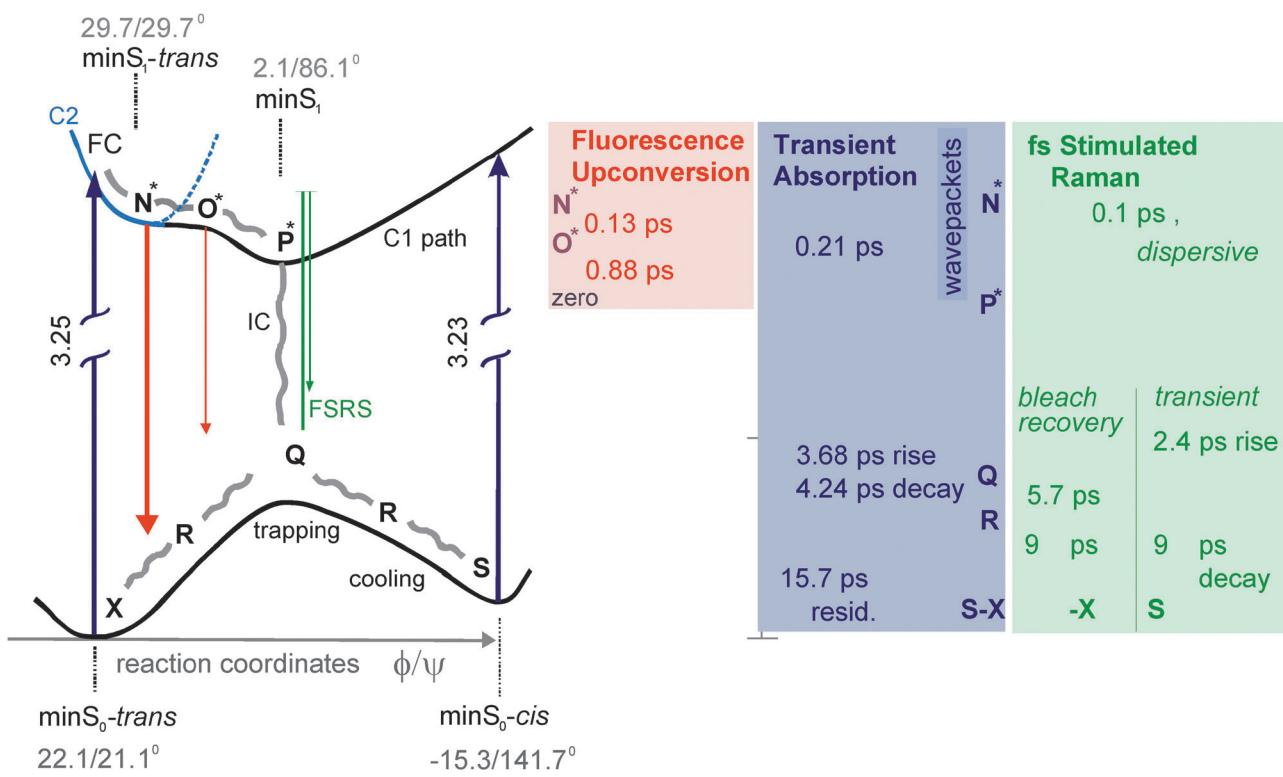


Fig. 11 Summary of quantum-chemical calculations (left) and observations (right).

Published on 17 July 2012. Downloaded by Michigan State University on 21/01/2016 02:31:41.

changes in  $\phi$  and  $\psi$  dihedrals while oscillating along totally symmetric modes. The  $C_2$  symmetry of the electronic ground state is approximately maintained during this initial phase. Then disrotatory motion  $\phi \approx -\psi$  sets in on a flat potential, leading to  $O^*$ . The process looks like the decay of a Gaussian distribution from a shelf or plateau; it is associated with the 0.13 ps spectral change observed by FLUPS and possibly with the 0.1 ps loss of FSRS intensity. Thereafter disrotatory motion continues to the global minimum  $\text{minS}_1$  which is associated with  $P^*$ . This excited “phantom state” is characterized by a perpendicular arrangement of the two moieties bound to the central C atom.  $P^*$  has a vanishing SE cross section and a weak and broad ESA. It is reached with a 0.9 ps time constant, corresponding to the decay time of the FLUPS signal. From there, internal conversion (3.7 ps) leads to a hot ground state  $Q$  as detected by TA measurements. Conversion is assisted by the slow component of solvent equilibration which brings the  $S_1$  and  $S_0$  surfaces closer. By FSRS we see that  $Q$  reaches its population peak at 5 ps. Simulations of steady-state vibrational RR spectra, compared to the measured FSRS spectrum at 5 ps, suggest the co-existence of hot precursors of both *cis* and *trans* forms in that state. Their contribution to the transient signal evolve in time, reflecting cooling on a 9 ps timescale. In this way the not-yet equilibrated separated isomers (collectively denoted  $R$ ) are prepared. Interestingly, the *trans* signal undergoes larger changes in time because of conversion of motions along non-symmetric modes in  $Q$ , to motions along symmetric modes in  $R$ . Upon further cooling the *cis* product state  $S$  is reached in 17–20% quantum yield, leaving the original *trans* ground-state partly bleached ( $-X$ ).

Even with the simplest cyanine and using a combination of three femtosecond broadband spectroscopies, we could not derive a picture of the barrierless photoisomerisation of 1122-P by observations alone. The more one measures, the less clear the picture seems to become (and conversely). Observations where however understood by complementing the analysis with quantum-chemical calculations of the participating PES. Specifically, we were able to map band envelopes and vibronic features of transient spectra to dynamical coordinates through classical simulations of the motion of an initial distribution along a minimum-energy reaction path, coupled with a pseudo-stationary treatment of fast vibrations. This approach seems to provide a practicable alternative to quantum molecular dynamics simulations on the  $S_1$  PES. From that perspective, it is worthwhile to concentrate foremost on accurate calculations of minimum-energy paths, or of reduced-dimensionality PES along the slowest coordinates. For example, a classical evolution on a 2D  $S_1$  PES along the  $\psi$  and  $\phi$  dihedrals would give hints on whether the second possible path, where disrotatory motion removes the symmetry immediately after photoexcitation, competes with the one described here.

## Acknowledgements

We thank the Deutsche Forschungsgemeinschaft for support (to NPE, through project ER154/10-1). FS thanks IIT (Project Seed HELYOS) and MIUR (PRIN2008 “TIME”); RI thanks MIUR (PRIN2008 and FIRB “Futuro in Ricerca” 2008).

## References

- 1 C. H. G Williams, *Trans. - R. Soc. Edinburgh*, 1856, **21**, 377.
- 2 D. Möbius, Scheibe Aggregates, *Adv. Mater.*, 1995, **7**, 437.
- 3 A. Mishra, R. K. Behera, P. K. Behera, B. K. Mishra and G. B. Behera, *Chem. Rev.*, 2000, **100**, 1973.
- 4 B. A. Armitage, *Top. Curr. Chem.*, 2005, **253**, 55.
- 5 M. Levitus and S. Ranjit, *Q. Rev. Biophys.*, 2011, **44**, 123.
- 6 H. Zollinger, *Color Chemistry*, Wiley-VCH, 3rd edn, 2003.
- 7 B. Bagchi, G. R. Fleming and D. W. Oxtoby, *J. Chem. Phys.*, 1983, **78**, 7375.
- 8 E. Åkesson, H. Bergström, V. Sundström and T. Gillbro, *Chem. Phys. Lett.*, 1986, **126**, 385.
- 9 S. Olsen and R. H. McKenzie, *J. Chem. Phys.*, 2009, **131**, 234306.
- 10 A. Sanchez-Galvez, P. Hunt, M. A. Robb, M. Olivucci, T. Vreven and H. B. Schlegel, *J. Am. Chem. Soc.*, 2000, **122**, 2911.
- 11 R. Improta and F. Santoro, *J. Chem. Theory Comput.*, 2005, **1**, 215.
- 12 P. A. Hunt and M. A. Robb, *J. Am. Chem. Soc.*, 2005, **127**, 5720.
- 13 D. Dietzek, B. Brüggemann, T. Pascher and A. Yartsev, *Phys. Rev. Lett.*, 2006, **97**, 258301.
- 14 D. Dietzek, T. Pascher and A. Yartsev, *J. Phys. Chem. B*, 2007, **111**, 6034.
- 15 D. Dietzek, N. Christensson, T. Pascher, T. Pullerits and A. Yartsev, *J. Phys. Chem. B*, 2007, **111**, 5396.
- 16 D. Dietzek, B. Brüggemann, T. Pascher and A. Yartsev, *J. Am. Chem. Soc.*, 2007, **129**, 13014.
- 17 D. Dietzek, B. Brüggemann, P. Persson and A. Yartsev, *Chem. Phys. Lett.*, 2008, **455**, 13.
- 18 D. Dietzek, A. N. Tarnovsky and A. Yartsev, *Chem. Phys.*, 2009, **357**, 54.
- 19 A. Yartsev, J.-L. Alvarez, U. Åberg and V. Sundström, *Chem. Phys. Lett.*, 1995, **243**, 281.
- 20 Q.-H. Xu and G. R. Fleming, *J. Phys. Chem. A*, 2001, **105**, 10187.
- 21 B. Dietzek, T. Pascher and A. Yartsev, *J. Phys. Chem. B*, 2007, **111**, 6034.
- 22 Z. Wei, T. Nakamura, S. Takeuchi and T. Tahara, *J. Am. Chem. Soc.*, 2011, **133**, 8205.
- 23 G. Vogt, G. Krampert, P. Niklaus, P. Nuernberger and G. Gerber, *Phys. Rev. Lett.*, 2005, **94**, 068305.
- 24 P. Nuernberger, G. Vogt, G. Gerber, R. Improta and F. Santoro, *J. Chem. Phys.*, 2006, **125**, 044512.
- 25 G. Vogt, P. Nuernberger, G. Gerber, R. Improta and F. Santoro, *J. Chem. Phys.*, 2006, **125**, 044513.
- 26 V. Karunakaran, J. L. Pérez-Lustres, L. Zhao, N. P. Ernsting and O. Seitz, *J. Am. Chem. Soc.*, 2006, **128**, 2954.
- 27 F. M. Hamer and M. I. Kelly, *J. Chem. Soc.*, 1931, 777.
- 28 L. G. S. Brooker and G. H. Keyes, *J. Am. Chem. Soc.*, 1935, **57**, 2488.
- 29 J. D. Turner, *Acta Crystallogr.*, 1955, **8**, 119.
- 30 G. S. Levinson, W. T. Simpson and W. Curtis, *J. Am. Chem. Soc.*, 1957, **79**, 4314.
- 31 S. G. Elkomoss, *J. Mol. Spectrosc.*, 1961, **7**, 14.
- 32 H. J. Friedrich, W. Gückel and G. Scheibe, *Chem. Ber.*, 1962, **95**, 1378.
- 33 E. Daltrozzo, G. Hohlneicher and G. Scheibe, *Ber. Bunsenges. Phys. Chem.*, 1965, **69**, 190.
- 34 I. Leubner, J. Dehler and G. Hohlneicher, *Ber. Bunsenges. Phys. Chem.*, 1967, **71**, 560.
- 35 G. Scheibe, E. Daltrozzo, O. Wörz and J. Heiss, *Zeitschrift für Physikalische Chemie*, 1969, **64**, 97.
- 36 P. J. Dynes, G. S. Chapman, E. Kebede and F. W. Schneider, *J. Am. Chem. Soc.*, 1972, **94**, 6356.
- 37 I. H. Leubner, *J. Org. Chem.*, 1973, **38**, 1098.
- 38 I. H. Leubner, *Org. Magn. Reson.*, 1974, **6**, 253.
- 39 A. L. Dobryakov, S. A. Kovalenko, A. Weigel, J. L. Pérez-Lustres, J. Lange, A. Müller and N. P. Ernsting, *Rev. Sci. Instrum.*, 2010, **81**, 113106.
- 40 R. Schanz, S. A. Kovalenko, V. Kharlanov and N. P. Ernsting, *Appl. Phys. Lett.*, 2001, **79**, 566; L. Zhao, J. L. Pérez Lustres, V. Farztdinov and N. P. Ernsting, *Phys. Chem. Chem. Phys.*, 2005, **7**, 1716; X.-X. Zhang, C. Würth, L. Zhao, U. Resch-Genger, N. P. Ernsting and M. Sajadi, *Rev. Sci. Instrum.*, 2011, **82**, 063108.
- 41 S. A. Kovalenko, A. L. Dobryakov and N. P. Ernsting, *Rev. Sci. Instrum.*, 2011, **82**, 063102.
- 42 Y. Yanai, D. P. Tew and N. C. Handy, *Chem. Phys. Lett.*, 2004, **393**, 51.

- 43 M. J. G. Peach, T. Helgaker, P. Salek, T. W. Keal, O. B. Lutnaes, D. J. Tozer and N. C. Handy, *Phys. Chem. Chem. Phys.*, 2006, **8**, 558.
- 44 J. Tomasi, B. Mennucci and R. Cammi, *Chem. Rev.*, 2005, **105**, 2999.
- 45 C. Manzoni, D. Polli and G. Cerullo, *Rev. Sci. Instrum.*, 2006, **77**, 023103.
- 46 D. Polli, L. Luer and G. Cerullo, *Rev. Sci. Instrum.*, 2007, **78**, 103108.
- 47 A. Weigel and N. P. Ernsting, *J. Phys. Chem. B*, 2010, **114**, 7879.
- 48 M. J. Frisch, G. W. Trucks, H. B. Schlegel, G. E. Scuseria, M. A. Robb, J. R. Cheeseman, G. Scalmani, V. Barone, B. Mennucci, G. A. Petersson, H. Nakatsuji, M. Caricato, X. Li, H. P. Hratchian, A. F. Izmaylov, J. Bloino, G. Zheng, J. L. Sonnenberg, M. Hada, M. Ehara, K. Toyota, R. Fukuda, J. Hasegawa, M. Ishida, T. Nakajima, Y. Honda, O. Kitao, H. Nakai, T. Vreven, J. A. Montgomery, Jr., J. E. Peralta, F. Ogliaro, M. Bearpark, J. J. Heyd, E. Brothers, K. N. Kudin, V. N. Staroverov, R. Kobayashi, J. Normand, K. Raghavachari, A. Rendell, J. C. Burant, S. S. Iyengar, J. Tomasi, M. Cossi, N. Rega, J. M. Millam, M. Klene, J. E. Knox, J. B. Cross, V. Bakken, C. Adamo, J. Jaramillo, R. Gomperts, R. E. Stratmann, O. Yazyev, A. J. Austin, R. Cammi, C. Pomelli, J. W. Ochterski, R. L. Martin, K. Morokuma, V. G. Zakrzewski, G. A. Voth, P. Salvador, J. J. Dannenberg, S. Dapprich, A. D. Daniels, Ö. Farkas, J. B. Foresman, J. V. Ortiz, J. Cioslowski and D. J. Fox, *Gaussian 09, Revision A.1*, Gaussian, Inc., Wallingford CT, 2009.
- 49 J. Fabian, *Dyes Pigm.*, 2010, **84**, 36.
- 50 D. Jacquemin, V. Wathelet, E. A. Perpète and C. Adamo, *J. Chem. Theor. Comput.*, 2009, **5**, 2420.
- 51 D. Jacquemin, Y. Zhao, R. Valero, C. Adamo, I. Ciofini and D. G. Truhlar, *J. Chem. Theory Comput.*, 2012, **8**, 1255.
- 52 R. Improta, V. Barone, G. Scalmani and M. J. Frisch, *J. Chem. Phys.*, 2006, **125**, 054103.
- 53 R. Improta, M. J. Frisch, G. Scalmani and V. Barone, *J. Chem. Phys.*, 2007, **127**, 74504.
- 54 F. Santoro, R. Improta, A. Lami, J. Bloino and V. Barone, *J. Chem. Phys.*, 2007, **126**, 084509.
- 55 F. Santoro, A. Lami, R. Improta and V. Barone, *J. Chem. Phys.*, 2007, **126**, 184102.
- 56 F. Santoro, R. Improta, A. Lami, J. Bloino and V. Barone, *J. Chem. Phys.*, 2008, **128**, 224311.
- 57 F. Santoro and V. Barone, *Int. J. Quantum Chem.*, 2010, **110**, 476.
- 58 F. Santoro, C. Cappelli and V. Barone, *J. Chem. Theory Comput.*, 2011, **7**, 1824.
- 59 F. Santoro, *FCclasses: A Fortran 77 Code*, 2008 (available via the Internet at <http://village.pi.iccm.cnr.it>; last accessed 13 July 2012).
- 60 V. Barone, J. Bloino, M. Biczysko and F. Santoro, *J. Chem. Theory Comput.*, 2009, **5**, 540.
- 61 J. Bloino, M. Biczysko, F. Santoro and V. Barone, *J. Chem. Theory Comput.*, 2010, **6**, 1256.
- 62 J. E. Heller, R. Sundber and D Tannor, *J. Phys. Chem.*, 1982, **86**, 1822.
- 63 A. Weigel, A. Dobryakov, B. Klaumünzer, M. Sajadi, P. Saalfrank and N. P. Ernsting, *J. Phys. Chem. B*, 2011, **115**, 3656.
- 64 M. Biczysko, J. Bloino, F. Santoro and V. Barone, in *Computational Strategies for Spectroscopy: from Small Molecules to Nanosystems*, ed. V. Barone, Wiley, Chichester, UK, 2011, pp. 361–446.
- 65 P. Van der Meulen, A. Jonkman and M. Glasbeek, *J. Phys. Chem. A*, 1998, **102**, 1906.
- 66 B. Bagchi and G. R. Fleming, *J. Phys. Chem.*, 1990, **94**, 9.
- 67 D. Braun, P. L. Nordio, A. Polimeno and G. Saielli, *Chem. Phys.*, 1996, **208**, 127.
- 68 H. Risken, *The Fokker-Planck Equation*, Springer Verlag, Berlin, 2nd edn, 1989.
- 69 J. Saltiel, *J. Am. Chem. Soc.*, 1967, **89**, 1036.
- 70 S. A. Kovalenko, A. L. Dobryakov, I. Ioffe and N. P. Ernsting, *Chem. Phys. Lett.*, 2010, **493**, 255.